文章编号：1001-9014(2021)05-0655-09

DOI：10. 11972/j. issn. 1001-9014. 2021. 05. 012

On-orbit non-uniformity correction method for infrared remote sensing systems using controllable internal calibration sources

SHENG Yi-Cheng[1,2], DUN Xiong[1], QIU Su[1*], LI Li[1], JIN Wei-Qi[1], WANG Xia[1]

(1. Beijing Institute of Technology, MOE Key Laboratory of Optoelectronic Imaging Technology and System, Beijing 100081, China;
2. Beijing Institute of Technology, Zhuhai 519088, China)

Abstract: Numerous detectors and the large time scale make non-uniformity correction (NUC) challenging for an infrared focal plane array. Typical calibration systems for infrared remote sensing systems block the full optical pupil and expose the sensor to an on-board calibration source (blackbody) and may also point to deep space as a calibration source. It is impractical (or expensive) to calibrate the high dynamic range remote sensing system with an on-orbit full aperture calibration source. This paper proposes and simulates an internal calibration system wherein a controllable internal calibration illumination is superimposed on the space imagery. The CICS-NUC method is applicable to the NUC when the calibration source adopts steady-state mode. After a comprehensive simulation analysis, an on-orbit NUC method based on the controllable internal calibration sources (CICS-NUC) is proposed using this type of calibrator. The proposed approach provides effective NUC without blocking the full optical pupil when the sensor stares at deep space. After executing the proposed NUC method, the non-uniformity of the evaluation image was reduced from an initial pre-correction value of 15. 87% to a post-NUC value of 1. 2%. The proposed approach has advantages of high efficiency, adaptability, and real-time processing. In addition, compared with the scheme of cutting a large extended blackbody into the imaging optical path, the simple structure and compact design of the internal calibration device reduce system costs.

Key words: infrared remote sensing, radiometric calibration, on-orbit, high dynamic range, scene-based non-uniformity correction

基于可控内定标源的星上红外遥感相机非均匀性校正方法

盛一成[1,2], 顿 雄[1], 裘 溯[1*], 李 力[1], 金伟其[1], 王 霞[1]

(1. 北京理工大学 光电学院,光电成像技术与系统教育部重点实验室,北京 100081;
2. 北京理工大学 珠海学院,广东 珠海 519088)

摘要:长时间工作或环境变化时,红外焦平面阵列器件易产生非均匀性的问题。典型的星上定标方法是将系统指向深空场景或在入瞳处引入星上面源黑体辐射。覆盖全口径的星上黑体普遍体积较大、设计复杂且成本高昂。为了解决这些难题,我们提出了一种基于可控内定标装置和星空场景的红外遥感系统星上非均匀性校正方法。该方法利用可控内定标源提供不同的靶面基准辐照度,通过计算获得不同辐射定标段的定标参数,覆盖探测器动态范围,实现不遮挡视场情况下的高动态范围非均匀性校正。通过模拟指向深空场景的在轨定标过程,并对模拟图像进行非均匀性校正,用于非均匀性校正的评价图像的非均匀性由初始的15.87%下降到1.2%以下。本方法具有快速、高效、鲁棒性强等优点且具有实时处理的前景。相比于需要引入星上面源黑体的定标方法,本系统的内定标装置结构简单、设计小型化且节省成本。

关 键 词:红外遥感;辐射定标;在轨;高动态范围;基于场景非均匀性校正

中图分类号:TP7　　**文献标识码**:A

Received date: 2019- 09- 19, **revised date**: 2021- 08- 29　　**收稿日期**:2019- 09- 19, **修回日期**:2021- 08- 29

Foundation items: This work was supported by the National Natural Science Foundation of China (61871034), the 13th Five-Year Plan Pre-study Foundation of the Army Armament Department of China (3010204004104) and the National Key R&D Program of China (2018YFB0504900).

Biography: SHENG Yicheng (1987-), male, Beijing, china, doctoral student at Beijing Institute of Technology. His current research interests include non-uniformity correction, radiometric calibration, small infrared target detection and electronic circuit design in remote sensing systems. E-mail: shengyicheng87@gmail. com

[*] **Corresponding author**: E-mail: edmondqiu@bit. edu. cn

Introduction

The Nonuniformity correction (NUC) is a crucial procedure for infrared remote sensing [1-2]. NUC (i. e., radiometric calibration in relative scale) can be broadly classified into two major categories: calibration-based techniques (CBNUC) and scene-based techniques (SBNUC) [3]. A typical CBNUC method uses a uniform onboard calibrator, e. g., a blackbody source, to block the full entrance pupil or switch the imaging optical path to the radiance source [4]. The uniform radiance of the source is projected onto the infrared focal plane array (IRFPA) and the calibration parameters are obtained by changing the calibrator's temperature [5, 6]. Typical CBNUC methods examined by existing literature include the one-point method [7], two-point method [8, 9], multipoint method [10, 11], and staircase-scene-based method [12]. These CBNUC methods are effective with the minimal algorithm complexity; however, it is difficult to adapt to an application system that cannot provide a very uniform scene illumination. In particular, owing to the larger aperture used by high-earth-orbit infrared remote sensing systems, it is impractical (or expensive) to calibrate the remote sensing system with a blackbody of the same size as the primary lens owing to the limitations of space, weight, and power consumption. There is a lack of high dynamic range (HDR) vacuum extended blackbody according to the CBNUC methods for the radiometric calibration of HDR infrared remote sensing system. Because of these physical constraints, CBNUC methods based on an external calibration source are not applicable in this special case. In contrast, SBNUC methods are designed to calculate the non-uniformity from IRFPA frames without a reference source and then compensate the dynamic non-uniformity [13]. Most of the current NUC research focuses on the SBNUC methods, including constant statistics based algorithms [14-17], least mean square methods [18], neural network based algorithms [19], and registration based methods [20-21]. These SBNUC algorithms estimate true scene radiance based on series of images or the frame-to-frame global motion, which typically have high requirements of computing input data regarding the dynamic scene and the local motion characteristics between scenes [21]. The imagery of a high-earth-orbit infrared remote sensing system has a deep-space as background during the calibration procedures, and it becomes impossible for the system to identify a dynamic scene or the motion characteristics of the scene that meet the assumption of the SBNUC algorithm. For the internal calibration scheme [22-24], the calibration optical paths must be separated from the telescope imaging optics during the on-orbit calibration procedure. In this procedure, the internal calibration sources (ICS) may generate non-uniformity and other unfavorable effects. Previously, we proposed an NUC method based on modulated internal calibration sources (MICS-NUC) combined with an SBNUC method to achieve a high dynamic range NUC [25]. However, this method requires the ICS to be modulated in the selected dynamic range. If the required modulation condition cannot be met, the processing algorithm is no longer applicable.

In this study, based on the optical structure of previous research [26], we propose an on-orbit NUC method based on the controllable internal calibration sources (CICS-NUC) for the HDR infrared remote sensing system. During the calibration process, we superimpose the ICS radiance onto the deep space background to construct an HDR scene while the system stares at deep space. After the correction process, calibration parameters are obtained and the CICS-NUC method can be implemented for the remote sensing system. The CICS-NUC method simplifies the ICS control system and the algorithm complexity, thus making the calibration easy to implement. In the following sections, the CICS-NUC method is introduced and verified with simulations.

1 NUC Method with CICS

MICS-NUC and CICS-NUC methods have the same on-orbit radiometric calibration device and system structure. The proposed push-room imaging high-earth-orbit system employs a linear dual-band IRFPA [25]. The ICS optical components occupy a hole in the main mirror within the central obscuration of the Schmidt telescope. The ICS optics are designed to operate synergistically with the Schmidt telescope's optics to produce a uniform and HDR light distribution at the IRFPA. The internal blackbody source of nichrome (HelioWorks, model EF8530) has three radiating fins with 1. 3% non-uniform illumination at the IRFPA [26]. The ICS operates in either pulsed or steady-state mode. The ICS in the proposed CICS-NUC method operates in a steady-state mode.

As bright stars are not conducive to the calibration process, their effect must be reduced. Another challenge is the difficulty encountered by the IRFPA when obtaining different levels of radiance directly from the space scene. Thus, the proposed approach uses a controllable ICS with various levels of radiance to obtain multiple calibration images for HDR calibration during the IRFPA scan. The on-orbit NUC based on controllable CICS-NUC method has two processing steps: a filtering process based on a local threshold and a segmentation two-point calibration based on a local mean. From the perspective of solving the key problems and the NUC image of the infrared system under the ICS operating in steady-state mode, the scene based adaptive NUC algorithm in this paper adopts the dynamic linear correction method. Figure 1 illustrates the processing flowchart of the proposed CICS-NUC method.

1.1 Filter the Image Outliers Based on a Local Threshold

As a few luminous stars within the deep-space background scene directly influence the estimation of the corrected true value, these sampled points must be filtered out. Furthermore, calibration images also contain other influential factors such as random noise of sensors and ICS illumination distribution non-uniformity. Therefore, the proposed algorithm adopts a filtering process based on a local threshold value. This approach discussed in the previous research (MICS-NUC) is to compute a

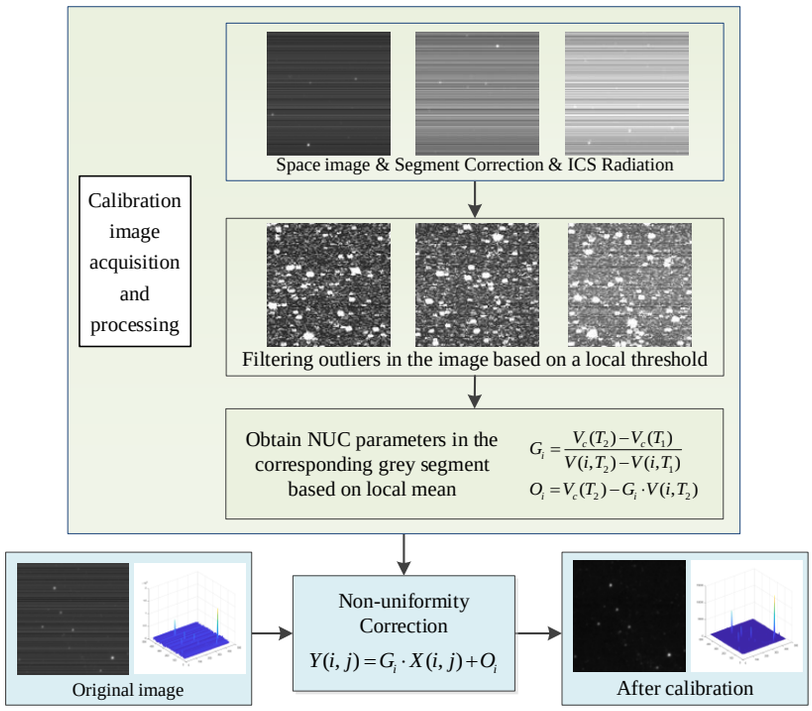

Fig. 1 Flow chart of the CICS-NUC method.
图1 CICS-NUC方法的流程图

threshold at every point (x, y) in the calibration image $f(x, y)$ based on two specified properties computed in a neighborhood s_{xy} [25]. Let σ_{xy} and m_{xy} denote the standard deviation and mean value of the set of pixels contained in a neighborhood (set as $1 \times d$ area), centered at coordinates (x, y). These two quantities are effective for determining local thresholds because they are descriptors of local contrast and average intensity. The evaluation method compares the local parameters (a and b) with the preset thresholds of m_{xy} and σ_{xy}; a point with a local parameter less than the threshold is an abnormal point. With the IRFPA scan (push-broom mode) horizontally, the corresponding local parameter calculation formula at the point (x, y) is

$$m_{xy} = \frac{1}{d}\sum_{s=-r}^{r} f(x,y+s)\ , \tag{1}$$

$$\sigma_{xy} = \left(\frac{1}{d}\sum_{s=-r}^{r}\left[f(x,y+s) - m_{xy}\right]^2\right)^{\frac{1}{2}}\ . \tag{2}$$

where r is the radius ($d = 2r + 1$), $x = 1, 2, \cdots, M$ and $y = 1, 2, \cdots, N$; M and N are the rows and columns in the image. By determining the point-by-point local thresholds of the image, an image $g(x, y)$ with marked outliers can be obtained.

$$g(x,y) = \begin{cases} 0 & \text{if} \quad \left|f(x,y) - m_{xy}\right| < a \quad \text{AND } \sigma_{xy} < b \\ f(x,y) & \text{otherwise} \end{cases}, \tag{3}$$

where a and b are the non-negative thresholds determined by experiments in advance. Note that in the section 2.2, the digital number of the marked point is ignored, the remaining pixels will be preserved as digital number of $g(x, y)$.

The parameter of the filtering process in the CICS-NUC method is determined by comparing the NUC effects in advance. The increase in the parameter d (the size of the neighborhood) not only increases the amount of calculation but also calculates another star, and therefore, the error increases. The parameter d should be close to the pixel size of the bright star; we set $d = 9$. The parameters a and b are descriptors of average intensity and local contrast, respectively. When b ranges from 10 to 13, and a ranges from 39 to 100, the NUC result at low gray-scale segments is optimal (gray-scale segments smaller than ICS-2000). The change of the parameters a and b do not have a large effect on the high gray-scale segments. This is because, when the system performs calibration operations for areas with fewer stars, the brighter pixels remaining after the filtering step will only have a greater impact on the calibration process of the low gray-scale. To better obtain the correction results of low gray-scale segments, $d = 9$, $a = 40$, and $b = 13$ are taken as the optimal local threshold parameters of the filtering process with various filtering parameters analysis. MICS-NUC and CICS-NUC methods have the same filtering process, but the parameter values of the two algorithms are not the same.

1.2 Segmentation Two-Point Calibration Based on Local Mean

Because of the HDR and the obvious nonlinear response of the system, the typical linear response model is no longer applicable. Therefore, according to the dynam-

ic range and calibration accuracy requirements, the IRFPA's dynamic range (R_{min}, R_{max}) is divided into K intervals (R_{k-1}, R_k), where $k = 1, 2, \cdots, K$, $R_0 = R_{min}$, and $R_K = R_{max}$. Calibration is executed respectively in each interval (segment) based on the linear response model. This paper takes the two-point algorithm as an example. According to the linear model, the size of the scanning IRFPA obtained is $M \times N$. Assume that the IRFPA NUC model is

$$Y(i,j) = G_i \cdot X(i,j) + O_i (i = 1,2,\cdots,M, j = 1,2,\cdots,N), \quad (4)$$

where G_i and O_i are the gain and offset parameters of the i–th channel, respectively, $X(i, j)$ is the original output image, and $Y(i, j)$ is the output image after NUC for the IRFPA. While the IRFPA is in the imaging process, the input radiance from the scene is used to select the corresponding NUC coefficients at each interval, and then complete the corresponding NUC according to the NUC equation.

The segmentation NUC can be executed in advance in the laboratory. When the on-orbit environment is simulated, the on-board controllable ICS provides reference radiance for segmentation calibration. The on-orbit segmentation interval and the calibration temperature points in the intervals are initially set during pre-launch calibration. The initial gain parameter G_{Lab} and offset parameter O_{Lab} can be continuously optimized according to the pre-launch calibration result. The segmentation interval, calibration point, and initial parameters are important coefficients for the subsequent calibration process.

A common algorithm to the NUC is to perform measurements with a blackbody source at two different absolute temperatures, T_1 and T_2, and then, to solve for the NUC coefficients. The average of the output values of all detectors is used as the corrected true value. This two-point method is performed using the global mean value as the corrected true value as follows:

$$\begin{aligned} V_c(i,T_1) &= G_i \cdot V(i,T_1) + O_i = V_c(T_1) \\ V_c(i,T_2) &= G_i \cdot V(i,T_2) + O_i = V_c(T_2)' \end{aligned} \quad (5)$$

where $V(i, T_1)$ and $V(i, T_2)$ are the mean values of the i-th channel in the calibration image of the temperatures T_1 and T_2, respectively, and $V_c(T_1)$ and $V_c(T_2)$ are the average of all channel output under the temperatures T_1 and T_2. Thus, the gain and offset parameters of IRFPA are

$$\begin{aligned} G_i &= \frac{V_c(T_2) - V_c(T_1)}{V(i,T_2) - V(i,T_1)} \\ O_i &= V_c(T_2) - G_i \cdot V(i,T_2) \end{aligned}. \quad (6)$$

Because the infrared camera is also affected by the weak background radiation of deep space, an NUC algorithm based on a local mean to obtain relative radiation calibration parameters is used. The parameters are obtained as follows:

The radiance of the ICS is used as a calibration source for an infrared remote sensing system; however, it will bring non-uniformity of illumination distribution of 1.3% through the calibration optical system [26]. The illumination from the ICS causes the radiance to be lower at the edge than at the center of the IRFPA, while it is simultaneously affected by the weak background radiance of deep space. Therefore, the periodic correction of the NUC algorithm during on-orbit calibration is required. The proposed method uses the local mean of the calibration image to determine the calibration parameters to reduce the effect of ICS illumination distribution (1.3%). The operating steps are as follows.

1) For one frame of the image at temperature T_1, the mean of each channel is averaged along the scanning direction. The mean of the effective value of the i-th channel is $V(i, T_1)$ and the group of all channels are set as matrix Q.

2) In the laboratory, NUC is processed using a standard blackbody source. After obtaining the initial NUC parameters, G_{Lab} and O_{Lab}, for each interval, matrix Q is corrected using the NUC parameters obtained in Step 1. Then, the corrected matrix Q constitutes matrix $Q1$.

3) To reduce the influence of weak background radiation, two-round mean filtering is executed on $Q1$ to obtain matrix $Q2$. The size of the filter is determined by the fluctuation of weak background radiation.

4) To eliminate the influence of ICS illumination distribution non-uniformity, $Q2$ is corrected according to the laboratory NUC parameters. The infrared system is aimed at the cold screen space simulator, the distribution of the ICS is calculated, and the mean value of the effective pixels of each channel is obtained. After normalizing, set the group of all channels as the matrix P. The non-uniformity distribution of the ICS is mapped to the matrix $Q2$ to obtain a local mean $V_{local}(T_1)$, as detailed in Eq. (7).

$$V_{local}(T_1) = P \cdot \frac{\max(Q2) - \min(Q2)}{1 - \min(P)} + \max(Q2) - \frac{\max(Q2) - \min(Q2)}{1 - \min(P)}. \quad (7)$$

The average value $V(i, T_2)$ and the local mean $V_{local}(T_2)$ of the effective pixels of the i-th channel of the calibration image of temperature T_2 are obtained in the same manner by repeating Steps 1 through 4. The local mean values, $V_{local}(T_1)$ and $V_{local}(T_2)$, are substituted for the global mean values $V_c(T_1)$ and $V_c(T_2)$ in Eq. (6) to obtain the calibration parameters of the interval.

The non-uniformity of the IRFPA changes with the operating state or environment, thus, a dynamic NUC is required. The system restarts the calibration process when the deviation becomes crosses a threshold determined by the algorithm and updates the calibration parameters accordingly. When the system is in observation mode, the ICS is turned off, and the IRFPA imaging data is subjected to NUC using Eq. (4) according to the NUC coefficients at each segmentation interval.

2 Verification and Results

To verify the efficacy of the CICS-NUC method, we analyzed and evaluated an implementation of the proposed algorithm on a simulation of on-orbit NUC for an infrared remote sensing system.

2.1 Simulation Images Acquisition

The simulated non-uniformity image was obtained by adding the influencing factors to the IRFPA during the radiometric calibration process while pointed at a specific area with a small number of stars exist in the deep space. The influencing factors included the controllable ICS illumination distribution [26], sensor fixed-pattern noise (FPN), and sensor random noise.

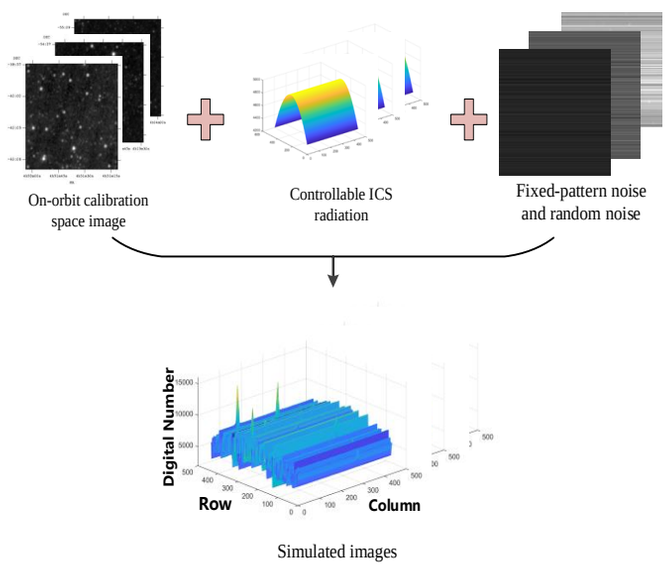

Fig. 2 Image data obtained by a scanning IRFPA with different ICS output (e. g. ICS equivalent output is 6000): the original space image data superposed with the ICS radiance, FPN, and random noise.

图2 不同ICS输出(如ICS等效输出灰度为6000时)的扫描型IRFPA所获得的图像数据:原始星空图像与ICS辐射、固定图案噪声、随机噪声进行叠加

Based on the assumptions that the infrared remote sensing system points to the deep space during the calibration process and that a small amount of star irradiance exists in the acquired calibration specific area, we selected an actual space scene from the Wide-field Infrared Survey Explorer mission (WISE) in the W2 band (4.36 μm) acquired from the NASA/IPAC Infrared Science Archive [27]. For the sake of comparison with the MICS-NUC method [25], we used the same original space scene.

Influential factors were added to the original space scene. Note that the following simulated images are all equivalent 14-bit gray-scale images. For the M channels of IRFPA, the output image $X_k(M)$ of each influencing factor was added to the space scene $S_k(M)$ below K intervals,

$$X_k(M) = [a_1(M) + a_{2k}(M) + 1]S_k(M) + [o_{2k}(M) + o_3(M)], \quad (8)$$

where $a_1(M)$ is the illumination non-uniformity of the ICS, $a_{2k}(M)$ is the gain of the sensor, $o_{2k}(M)$ is the offset of the sensor, and $o_3(M)$ is the random noise of the sensor.

We assumed that $a_1(M)$ followed a Gaussian distribution; then,

$$a_1(M) = \exp\left(-\frac{(x-\mu)}{2\sigma^2}\right). \quad (9)$$

The position parameter and the scale parameter are set at $\mu = 218$ and $\sigma = 300$, respectively. As a result, the illumination from the ICS caused the radiance at the edge of the IRFPA to be approximately 0.88 times that of the center of the IRFPA. Taking the ICS equivalent radiance output at 6000 for example, the original space image with the ICS radiance distribution is obtained after the scanning of the IRFPA.

We also assumed that the sensor's gain $a_{2k}(M)$ and sensor's offset $o_{2k}(M)$ followed a Gaussian random distribution with means of 1 and 850, and standard deviations of 0.17 and 350, respectively. The sensor's random noise $o_3(M)$ conformed to a Gaussian distribution with a mean of 0 and a standard deviation of 10. Based on the Equation (8), Fig. 2 shows the data obtained by superimposing various influential factors and a steady-mode ICS equivalent radiance output at 6000 (and other ICS equivalent outputs) using a scanning IRFPA.

2.2 Algorithm Process and Effects

2.2.1 Filtering on the Image

During the simulation of the on-orbit radiometric calibration, when the system pointed to the deep space scene, superposed calibration images of deep space and the multistage internal calibration radiance with the scanning process were obtained for the CICS-NUC method. Figure 3 shows the image obtained by the IRFPA when the original deep space image was superimposed with an ICS center radiance of equivalent gray-scale output at 500, 2000, 3000, 5500, and 6000. The local parameters were set (the length of the neighborhood d as 9 pixels, $a = 40$, and $b = 13$) and the filtering process was performed according to Equation (3). Figure 4 shows how the outliers in the simulated image were marked during filtering. As shown in Fig. 4, the outlier in the simulated image Fig. 3 is marked (the white part is an outlier). The algorithm can effectively mark most of the stars or nebulas.

2.2.2 NUC Results and Analysis

The deep space scene is not a uniform scene. For evaluating and analyzing the calibration results of the CICS-NUC algorithm, we also simulated a series of test images with the ideal uniform output at the IRFPA (gray-scale baseline equivalent output of 500~10000). The fixed-pattern noise distribution in the test images is the same as that in the simulated images (according to the same model, Equation (8)). Figure 5 shows two test images with the same FPN distribution as the aforementioned simulation images. The equivalent gray-scale output of Fig. 5(a) and 5(b) is 1500 and 5000, and the NU is 19.15% and 15.87%, respectively.

The test image has the same NUC operation; thus, the change of the test image non-uniformity (NU) also shows the effect of the CICS-NUC algorithm process.

Note that the evaluation parameter, NU, is given as follows:

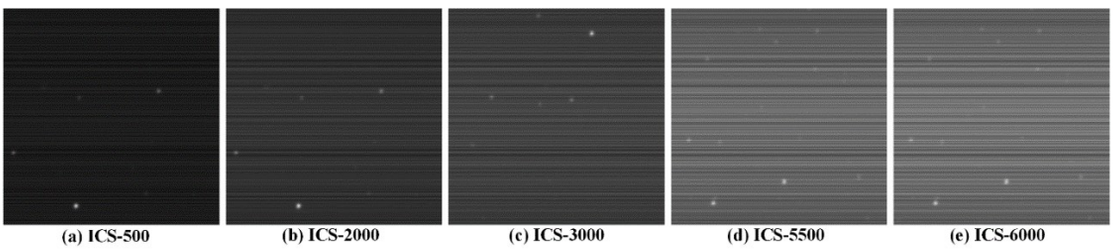

Fig. 3 Images ($f(x, y)$) obtained before the NUC by superposing various influence factors and a controllable steady-mode ICS equivalent output at 500, 2000, 3000, 5500, and 6000.
图3 在非均匀性校正之前,通过叠加各种影响因素和稳态模式ICS等效输出得到的图像(f(x, y)),ICS等效输出分别为500、2000、3000、5500和6000。

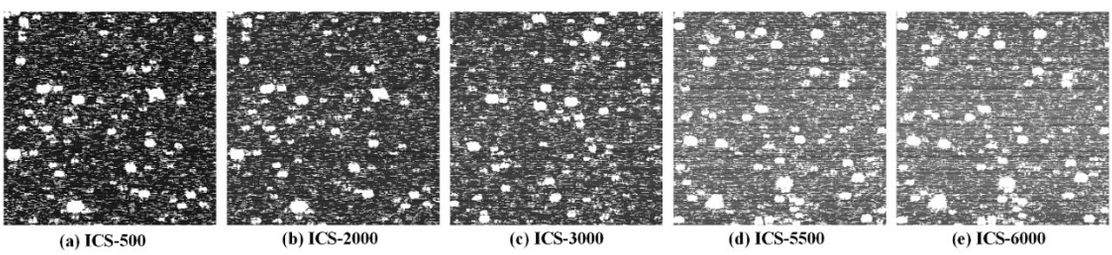

Fig. 4 Figure 3′s outlier is marked during the filtering process.
图4 图3中的异常值在滤波过程中被标记。

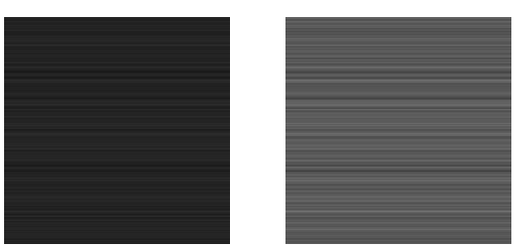

Fig. 5 Evaluation images for the validation process: (a) gray-scale baseline equivalent output of 1500, NU = 19.15%; (b) gray-scale baseline equivalent output of 5000, NU = 15.87%.
图5 测试评价图像: (a) 等效辐射输出为1500,NU = 19.15%; (b) 等效辐射输出为5000,NU = 15.87%

$$NU = \frac{1}{V_{avg}}\sqrt{\frac{1}{M \times N - (D + H)}\sum_{i=1}^{M}\sum_{j=1}^{N}(V_{ij} - V_{avg})^2}\ ,$$

$$V_{avg} = \frac{1}{M \times N - (D + H)}\sum_{i=1}^{M}\sum_{j=1}^{N}V_{ij} \quad , \quad (10)$$

where M and N are the total number of rows and columns of the IRFPA, respectively; D is the number of dead pixels in the IRFPA; H is the number of overheated pixels in the IRFPA; and V_{ij} is the corresponding pixel out of row i and column j on the IRFPA. The average of all effective pixels' output on the IRFPA is designated by V_{avg}. When calculating the sum and NU of the outputs, the values of the invalid pixels were not included.

The difference between using the global mean method and the local mean method is the estimation of the corrected true value. Two-point correction was performed with ICS equivalent gray-scale output 2000 and 6000 as calibration points. The correction was executed using global mean and local mean methods. The correction parameters obtained by different statistics methods were used to evaluate the NU of a series of test images. Figure 6 shows the post-NUC results of the test image (Fig. 5 (b)), and the local mean method has better effect. Note that intensity transformation is executed to display the corrected image. The corrected non-uniformity evaluation data for a series of test images is shown in Fig. 7.

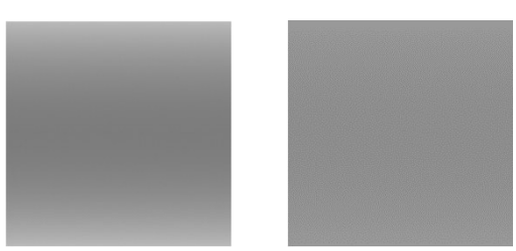

Fig. 6 With the ICS radiation at 2000 and 6000 as the calibration points, the correction results of Fig. 5b are evaluated by different algorithms: (a) global mean two-point correction algorithm; (b) local mean two-point correction algorithm.
图6 以ICS辐射等效输出2000和6000做为非均匀校正点,采用不同算法对测试评价图5b的校正结果进行评价:(a)采用全局均值两点校正算法的校正结果; (b)采用局部均值两点校正算法的校正结果

The high dynamic range IRFPA has the effect of response nonlinearity. To further reduce residual non-uniformity, corrections were implemented using the segment method. With the ICS equivalent gray-scale output at interval 500 – 3000 and interval 3000 – 5500 as the cali-

bration points, the two-point method based on the local mean was corrected for the two different correction intervals. The correction parameters obtained by the different intervals were used to evaluate the NU of a series of test images. The non-uniformity evaluation data of the test images is shown in Fig. 8. The non-uniformity evaluation results of Fig. 5 following NUC processing are summarized in Table 1. The NUC was more effective when a local mean value was adopted as the correction truth value, rather than when using a global mean. As indicated in Fig. 6, Fig. 7, and Table 1, the NU of the test images decreased from the initial 19.15% and 15.87% to 0.68% and 1.18%, respectively, which was better than 3.24% and 6.06% for the global mean correction algorithm. The overall image achieved a uniform and consistent effect that considerably improved image quality. This indicates that the proposed CICS-NUC method substantially improved the accuracy of the estimated NUC gain and offset in the correction of the illumination non-uniformity introduced by ICS. Not only did this realize the effective NUC of the IRFPA sensor, it also partially corrected the illumination NU of ICS. This proves that the estimate of the true mean value depends on the uniformity of the scene, that is, the image after removing the outliers, and the non-uniformity of ICS itself. The NU of ICS plays a major role when using the global mean as the corrected truth value. When the local mean value was used as the corrected truth value, the NU of ICS was considerably weakened, which helped improve the accuracy of calculating the calibration parameters.

As indicated in Fig. 8 and Table 1, compared with the different calibration interval, considering the test point to be 1500 as an example, when the ICS calibration interval is 500~3000, the correction result is less than the result at an interval of 2000~6000 (0.64% is better than 0.68%). This indicated that the segment correction of the CICS-NUC algorithm in Section 2.2 was effective because the NUC parameters obtained in the selected gray-scale achieved an improvement in the correction effect compared to those from other gray-scale segments. This indicates that an effective interval segmentation algorithm is crucial to the process. In addition, as shown in Fig. 8 and Table 1, with the ICS radiation at 2000 - 6000 as the calibration interval, the calibration results are similar to the calibration results when ICS radiation is 3000~5500. The correction intervals and calibration points need to be optimized based on the detector response curves and correction results. In fact, the correction method is a fitting process that requires repeated testing based on the results.

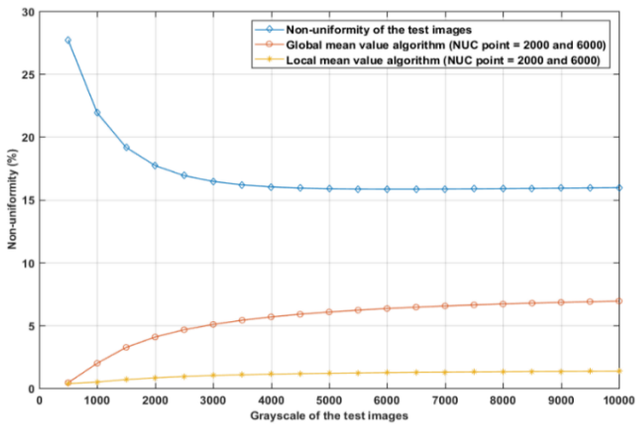

Fig. 7 Non-uniformity evaluation before and after NUC of each test image.
图7 采用不同校正方法对不同的测试评价图像进行非均匀性校正结果对比。

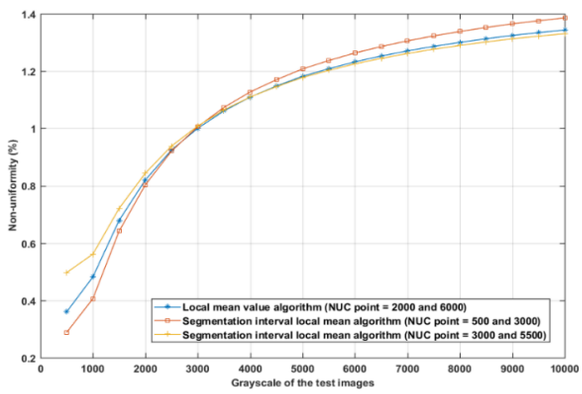

Fig. 8 NUC evaluation of test images by using different segmentation interval local mean algorithms.
图8 利用不同的灰度区间局部均值算法对评价图像进行非均匀性校正后的结果

To obtain the visual effect of the CICS-NUC on the actual deep space scenes, a WISE W2 band image located at 323.841, 1.48141 J2000 was added to FPN to simulate an original image before correction, as shown in Fig. 9(a). After performing NUC, the result is shown in Fig. 9(b). It shows that when the ICS equivalent output was 2000 and 6000 and these were selected as the cali-

Table 1 Non-uniformity correction (NUC) results from the test images in Fig. 5.
表1 图5测试评价图像的非均匀性校正效果评价

NUC algorithms		Non-uniformity of the test image after NUC (ICS-1500, NU = 19.15%)	Non-uniformity of the test image after NUC (ICS-5000, NU = 15.87%)
Internal calibration sources output as calibration points	Algorithm adopted		
2000 and 6000	Global mean value algorithm	3.24%	6.06%
2000 and 6000	Local mean value algorithm	0.68%	1.18%
500 and 3000	Segmentation interval local mean algorithm	0.64%	1.21%
3000 and 5500	Segmentation interval local mean algorithm	0.72%	1.17%

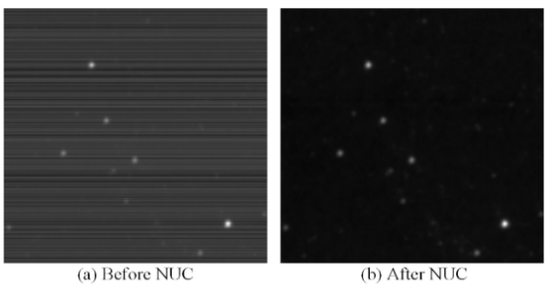

Fig. 9 Implementing the proposed CICS-NUC algorithm on an actual space scene.
图9叠加实际星空场景后的CICS-NUC算法校正效果

bration points, the CICS-NUC algorithm may be implemented to obtain the correction parameters. Note that intensity transformation is executed to display the corrected image. As observed in Fig. 9, the stripe-like and irregular non-uniform noise in the original image were successfully corrected by the propose NUC method.

3 Discussion

MICS-NUC method and CICS-NUC method are based on ICS operated in different modes (pulsed or steady-state mode). The ICS calibration system constructs the calibration images, thus meets the requirements of the SBNUC algorithms. After the variable threshold process of filtering outliers, the on-orbit HDR radiometric calibration can be finished by both of the two methods without blocking the field of view. Both algorithms can not only achieve effective NUC, but also partially correct the non-uniformity of ICS illumination irradiance. By utilizing the same NU response model to create a series of simulated images as test images, the correction effect of the two methods is compared. The correction results are shown in Fig. 10. It can be seen that:

1) The correction effect of CICS-NUC method is comparable to the MICS-NUC method in the whole dynamic range. The MICS-NUC method shows better NUC results than the CICS-NUC method at the medium gray level (the grayscale segment is 2000 to 4500) and the high grayscale (the grayscale segment is 4500 to 10000). The CICS-NUC method with calibration points of ICS-500 and ICS-2000 shows better NUC results than the MICS-NUC method with calibration point of ICS-1000 at the low grayscale (the grayscale segment is below 2000).

2) The NUC parameters obtained in the selected greyscale using the MICS-NUC and CICS-NUC methods have a better correction effect than those from other greyscale segments. The calibration point ICS-1000 shows better correction results in the low gray level (the grayscale segment is below 2000) than the MICS-NUC method using the calibration point ICS-2000. Therefore, the selection of the calibration point is crucial to the CICS-NUC method, and the CICS-NUC method obeys the same rules.

Through the comparison test, taking three segmentation intervals as an example, the MICS-NUC method (pulsed mode) using the local constant statistical algorithm requires three calibration points to obtain the calibration parameters. However, CICS-NUC method (steady-state mode) which adopts the local mean based algorithm requires at least four calibration points. Also, there are differences in the processing procedure: the ICS of the MICS-NUC method needs to be set within a certain range, and higher requirements are imposed on the ICS control. But the CICS-NUC method adopts a steady-state mode, which makes the ICS control simple and stable. Compared with the MICS-NUC based on constant statistics algorithm, the CICS-NUC algorithm requires fewer scan columns of the calibration images, resulting an easier engineering implementation. In summary, the two methods are feasible NUC methods with different ICS operating modes. In different ICS operating modes (pulsed mode and steady state mode), the correction effects are also different, and there are different application occasions.

The simulation images of this paper superimpose various factors that may affect the radiometric calibration of the infrared remote sensing system, so that they have enough authenticity and can basically conform the actual situation of the system. The simulation images are corrected independently, and the result shows the validity of

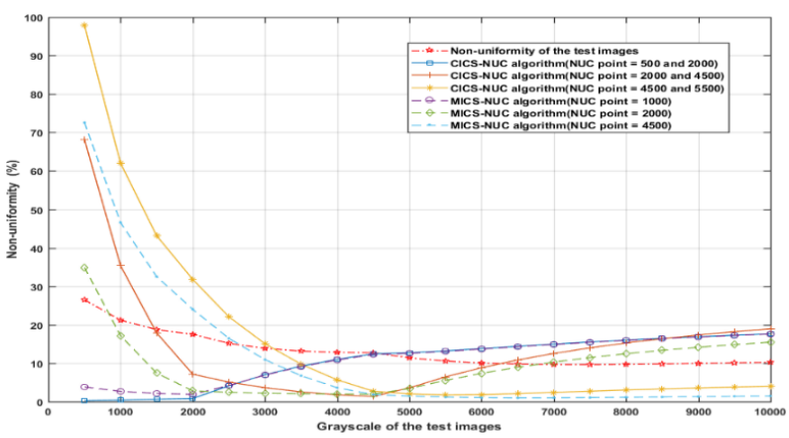

Fig. 10 NUC evaluation of test images by using MICS-NUC and CICS-NUC algorithms.
图10 MICS-NUC与CICS-NUC方法对一系列测试评价图像的校正结果

the algorithm. This method has important reference value for the design of the actual system. Of course, there are errors or secondary effective factors in this process, and it is necessary to improve it through experiments.

4 Conclusions

In this study, we proposed the CICS-NUC method to solve the problem of response non-uniformity of IRFPA in infrared remote sensing without blocking the entrance pupil. A detailed implementation of the proposed method was introduced, including segmentation, space scene and controllable ICS image acquisition, a variable threshold function for filtering outliers, local mean based two-point NUC, and other algorithms. Verification with simulated images demonstrated that the non-uniformity of the IRFPA was greatly reduced. Compared with other on-board NUC methods requiring reference sources (e. g., the CBNUC methods) and previous modulated internal calibration source based NUC methods, our CICS-NUC method has the advantages of miniaturization, ease of control and engineering implementation, fewer column scans, less computation, and thus, lower cost. The CICS-NUC method provides an effective solution for the on-orbit HDR dynamic calibration of a scanning IRFPA. We believe the implementation of this calibration method will meet the unmet demands of remote sensing systems in defense, meteorology and several other fields.

Acknowledgment

We sincerely thank Zhou Feng and Xiao Si from Beijing Institute of Space Mechanics & Electricity for their help in the research.

References

[1] J.M. Mooney, F.D. Shepherd. Characterizing IR FPA nonuniformity and IR camera spatial noise [J]. *Infrared Phys. Technol*. 1996, **37**(5): 595-606.
[2] J. Tansock, D. Bancroft, J. Butler, C. Cao, *et al*. Guidelines for Radiometric Calibration of Electro-Optical Instruments for Remote Sensing [M] Logan, UT, USA :Space Dynamics Lab Publications, 2015.
[3] M. Jin, W. Jin, Y. Li, S. Li. An evaluation method based on absolute difference to validate the performance of SBNUC algorithms [J]. *Infrared Phys. Technol*. 2016, **78**: 1-12.
[4] M. Montanaro, A. Lunsford, Z. Tesfaye, B. Wenny, D. Reuter. Radiometric calibration methodology of the Landsat 8 Thermal Infrared Sensor [J]. *Remote Sens*. 2014, **6**(9): 8803-8821.
[5] X. Chun. A flux calibration method for remote sensing satellites using star flux [J]. *J. Infrared Millim. Waves*, 2017, **36**(5): 581-588.
[6] X. Xiong, A. Angal, W. L. Barnes, *et al*. Updates of Moderate Resolution Imaging Spectroradiometer on-orbit calibration uncertainty assessments [J]. *J. Appl. Remote Sens*. 2018, **12**(3): 1-18.
[7] W. Qian, Q. Chen, G. Gu, Z. Guan. Correction method for stripe nonuniformity [J]. *Appl. Opt*. 2010, **49**(10): 1764-1773.
[8] R. Datla, X. Shao, C. Cao, X. Wu. Comparison of the calibration algorithms and si traceability of MODIS, VIIRS, GOES, and GOES-E RABI sensors [J]. *Remote Sens*. 2016, **8**(2): 126.
[9] S. Kim. Two-point correction and minimum filter-based nonuniformity correction for scan-based aerial infrared cameras [J]. *Opt. Eng*. 2012, **51**(10): 106401.
[10] M. Montanaro, R. Levy, B. Markham. On-Orbit Radiometric Performance of the Landsat 8 Thermal Infrared Sensor [J]. *Remote Sens*. 2014, **6**(12): 11753-11769.
[11] A. Gerace, M. Montanaro, R. Connal. Leveraging intercalibration techniques to support stray-light removal from Landsat 8 thermal infrared sensor data [J]. *J. Appl. Remote Sens*. 2017, **12**(01): 1-13.
[12] L. Huo, D. Zhou, D. Wang, R. Liu, B. He. Staircase-scene-based nonuniformity correction in aerial point target detection systems [J]. *Appl. Opt*. 2016, **55**(25): 7149-7156.
[13] W.T. Black, J.S. Tyo. Improving feedback-integrated scene cancellation nonuniformity correction through optimal selection of available camera motion [J]. *J. Electron. Imaging*. 2014, **23**(5): 053014.
[14] M.M. Hayat, S.N. Torres, E. Armstrong, S.C. Cain, B. Yasuda. Statistical algorithm for nonuniformity correction in focal-plane arrays [J]. *Appl. Opt*. 1999, **38**(5): 772-780.
[15] C. Zuo, Q. Chen, G. Gu, X. Sui, W. Qian. Scene-based nonuniformity correction method using multiscale constant statistics [J]. *Opt. Eng*. 2011, **50**(8): 087006-087011.
[16] J.G. Harris, Y. Chiang. Nonuniformity Correction of Infrared Image Sequences Using the Constant-Statistics Constraint [J]. *IEEE* Trans. Image Process. 1999, **8**(8): 1148-1151.
[17] C. Zhang, W. Zhao. Scene-based nonuniformity correction using local constant statistics [J]. *JOSA A*. 2008, **25**(6): 1444-1453.
[18] R.C. Hardie, F. Baxley, B. Brys, P. Hytla. Scene-Based Nonuniformity Correction with Reduced Ghosting Using a gated LMS Algorithm [J]. *Opt. Express* 2009, **17**(17): 14918.
[19] D.A. Scribner, K.A. Sarkady, J.T. Caulfield, M.R. Kruer, G. Katz, C. Gridley, C. Herman. Nonuniformity correction for staring ir focal plane arrays using scene-based techniques [C]. Applications of Artificial Neural Networks, International Society for Optics and Photonics, Orlando, FL, USA, 1990, **1308**: 224-233.
[20] R.C. Hardie, M.M. Hayat, E. Armstrong, B. Yasuda. Scene-based nonuniformity correction with video sequences and registration [J]. *Appl. Opt*. 2000, **39**(8): 1241-1250.
[21] W. T. Black, J. S. Tyo. Feedback-integrated scene cancellation scene-based nonuniformity correction algorithm [J]. *J. Electron. Imaging* 2014, **23**(2): 023005.
[22] E.C. Kintner, W.K. Wong, E.S. Jacobs, P.J. Cucchiaro, R.J. Koshel. Efficient and versatile internal reference sources for remote sensing space telescopes [C]. Infrared Spaceborne Remote Sensing, International Society for Optical Engineering, San Diego, California, USA, 2006, **6297**: p. 62970F.
[23] E.C. Kintner, J.M. Hartley, E.S. Jacobs, P.J. Cucchiaro. Advanced development of internal calibration sources for remote sensing telescopes [C]. Infrared Spaceborne Remote Sensing, International Society for Optics and Photonics, Denver, USA, 2004, **5543**: 313-319.
[24] E.C. Kintner, E.S. Jacobs, J.M. Hartley, P.J. Cucchiaro, L. Wall. Infrared Internal Calibration Sources developed at SSGPO, inc. [C]. Infrared Spaceborne Remote Sensing, International Society for Optics and Photonics, San Diego, California, USA, 2003, 5152: pp. 42-50.
[25] Y. Sheng, X. Dun, W. Jin, F. Zhou, X. Wang, F. Mi, S. Xiao. The On-Orbit Non-Uniformity Correction Method with Modulated Internal Calibration Sources for Infrared Remote Sensing Systems [J]. *Remote Sens*. 2018, **10**(6): 830.
[26] Y. Sheng, W. Jin, X. Dun, F. Zhou, S. Xiao. A design of an on-orbit radiometric calibration device for high dynamic range infrared remote sensors [C], AOPC 2017: Space Optics and Earth Imaging and Space Navigation, International Society for Optics and Photonics, Beijing, China, 2017, p. 104631N.
[27] Wide-field Infrared Survey Explorer, [EB/OL]. [2019] https://irsa.ipac.caltech.edu/applications/wise/